



HAL
open science

Perinuclear distribution of heterochromatin in developing *C. elegans* embryos.

Jeremy Grant, Craig Verrill, Vincent Coustham, Alain Arnéodo, Francesca Palladino, Karine Monier, André Khalil

► To cite this version:

Jeremy Grant, Craig Verrill, Vincent Coustham, Alain Arnéodo, Francesca Palladino, et al.. Perinuclear distribution of heterochromatin in developing *C. elegans* embryos.. *Chromosome Research*, 2010, 18 (8), pp.873-85. 10.1007/s10577-010-9175-2 . hal-02662919

HAL Id: hal-02662919

<https://hal.inrae.fr/hal-02662919>

Submitted on 31 May 2020

HAL is a multi-disciplinary open access archive for the deposit and dissemination of scientific research documents, whether they are published or not. The documents may come from teaching and research institutions in France or abroad, or from public or private research centers.

L'archive ouverte pluridisciplinaire **HAL**, est destinée au dépôt et à la diffusion de documents scientifiques de niveau recherche, publiés ou non, émanant des établissements d'enseignement et de recherche français ou étrangers, des laboratoires publics ou privés.

Perinuclear distribution of heterochromatin in developing *C. elegans* embryos

Jeremy Grant · Craig Verrill · Vincent Coustham ·
Alain Arneodo · Francesca Palladino ·
Karine Monier · Andre Khalil

Received: 10 August 2010 / Accepted: 16 November 2010 / Published online: 30 November 2010
© Springer Science+Business Media B.V. 2010

Abstract Specific nuclear domains are nonrandomly positioned within the nuclear space, and this preferential positioning has been shown to play an important role in genome activity and stability. Well-known examples include the organization of repetitive DNA in telomere clusters or in the chromocenter of *Drosophila* and mammalian cells, which may provide a means to

control the availability of general repressors, such as the heterochromatin protein 1 (HP1). We have specifically characterized the intranuclear positioning of in vivo fluorescence of the *Caenorhabditis elegans* HP1 homologue HPL-2 as a marker for heterochromatin domains in developing embryos. For this purpose, the wavelet transform modulus maxima

Responsible Editor: Mary Delany

Electronic supplementary material The online version of this article (doi:10.1007/s10577-010-9175-2) contains supplementary material, which is available to authorized users.

J. Grant · A. Khalil (✉)
Department of Mathematics and Statistics,
University of Maine,
Orono, ME 04469, USA
e-mail: andre.khalil@maine.edu

J. Grant · A. Khalil
Graduate School of Biomedical Sciences,
University of Maine,
Orono, ME 04469, USA

C. Verrill
Department of Electrical and Computer Engineering,
University of Maine,
Orono, ME 04469, USA

V. Coustham · A. Arneodo · F. Palladino · K. Monier
Université de Lyon,
F69007 Lyon, France

V. Coustham · F. Palladino
Laboratoire de Biologie Moléculaire de la Cellule,
École Normale Supérieure de Lyon,
Lyon, France

A. Arneodo · K. Monier
Laboratoire Joliot-Curie,
École Normale Supérieure de Lyon,
Lyon, France

A. Arneodo
Laboratoire de Physique,
École Normale Supérieure de Lyon,
Lyon, France

A. Khalil
Department of Physics and Astronomy,
University of Maine,
Orono, ME 04469, USA

A. Khalil
Institute for Molecular Biophysics, University of Maine,
Orono, ME 04469, USA

Present Address:
V. Coustham
John Innes Centre,
Colney,
Norwich NR4 7UH, UK

(WTMM) segmentation method was generalized and adapted to segment the small embryonic cell nuclei in three dimensions. The implementation of a radial distribution algorithm revealed a preferential perinuclear positioning of HPL-2 fluorescence in wild-type embryos compared with the diffuse and homogeneous nuclear fluorescence observed in the *lin-13* mutants. For all other genotypes analyzed, the quantitative analysis highlighted various degrees of preferential HPL-2 positioning at the nuclear periphery, which directly correlates with the number of HPL-2 foci previously counted on 2D projections. Using a probabilistic 3D cell nuclear model, we found that any two nuclei having the same number of foci, but with a different 3D probabilistic positioning scheme, can have significantly different counts in the 2D maximum projection, thus showing the deceptive limitations of using techniques of 2D maximum projection foci counts. By this approach, a strong perinuclear positioning of HPL-2 foci was brought into light upon inactivation of conserved chromatin-associated proteins, including the HAT cofactor TRAPP.

Keywords nuclear architecture · heterochromatin · *C. elegans* · 3D image analysis · wavelet transform · segmentation · modeling

Abbreviations

2D	Two-dimensional
3D	Three-dimensional
DNA	Deoxyribonucleic acid
GFP	Green fluorescent protein
HAT	Histone acetyl transferase
HDAC	Histone deacetylase complex
HDA	Histone deacetylase
HP1	Heterochromatin protein 1
HPL-2	Heterochromatin protein-like 2
kb	Kilobase
Mi-2/NuRD	NUcleosome remodeling and histone Deacetylase
Muv	Multivulval
μm	Micrometer
nm	Nanometer
PI3K	Phosphatidyl-inositol-3-kinase
Rb	Retinoblastoma
RNA	RiboNucleic acid
RNAi	RNA interference
SIR	Silencing information regulator
synMuv	Synthetic multivulval

TIP60/NuA4	histone acetyltransferase complex
TRRAP	Transformation/transcription domain-associated protein
TSA	Trichostatin A
WT	Wavelet transform
WTMM	Wavelet transform modulus maxima

Introduction

Over the past few decades, cell nuclear architecture has been widely studied, and several milestones have been reached, leading to a better understanding of the preferential positioning and function of nuclear domains. For example, mammalian interphase chromosomes have been shown to occupy discrete structural and functional territories (Cremer et al. 2000, 2001; Dundr and Misteli 2001; Gilbert et al. 2005; Cook and Marenduzzo 2009). The possible functional importance of the positioning and even the morphology of nuclear domains in general remains poorly understood although recent progress from novel image processing and numerical modeling methods have provided new insights (Brianna Caddle et al. 2007; Khalil et al. 2007; Cook and Marenduzzo 2009; de Nooijer et al. 2009). Adequate quantitative methods to measure or correlate various aspects of chromosomal structure, particularly in a normal 3D interphase context are still needed.

In animal nuclei, specific domains have been found localized close to nucleoli in a cell cycle (Ferguson and Ward 1992; Vourc'h et al. 1993), as well as in a differentiation dependent manner (Chaly and Munro 1996). Likewise, in differentiated nuclei, dense-stained, transcriptionally inactive heterochromatin is not distributed randomly in the nucleus, but is usually found against the inner face of the nuclear membrane. It has been suggested that a preferential peripheral positioning of heterochromatin is a consequence of its interactions with lamina proteins (Ye et al. 1997; Solovei et al. 2004; Fang and Spector 2005; Cook and Marenduzzo 2009). In yeast, telomere clustering at the nuclear envelope mediated by the telomerase-binding factor yeast Ku helps protect telomeric repeats from recombination (Buhler and Gasser 2009). However, recent developments in numerical simulation algorithms suggest that entropic forces could be responsible for many of the observed

preferential positioning of nuclear domains, like heterochromatin or nucleoli, by the principle of depletion attraction (Cook and Marenduzzo 2009; de Nooijer et al. 2009). In particular, applied molecular dynamics to Arabidopsis interphase nuclei revealed that non-specific interactions are sufficient to account for the preferential positioning of heterochromatin at the nuclear periphery (de Nooijer et al. 2009). Therefore, entropic forces can by themselves explain the preferential localization of heterochromatin domains. The authors go on to suggest that interactions between lamina proteins and heterochromatin may further stabilize this localization in animals and may be important to keep heterochromatin away from nucleopores, where active transcription occurs (Taddei 2007).

The clustering of repetitive DNA in foci such as telomere clusters or in the chromocenter of *Drosophila* or mammalian cells may also provide the cell with a means to control the availability of general repressors, such as SIR factors, Ikaros, or the context dependent transcriptional repressor HP1. HP1 family proteins are essential components of constitutive heterochromatin in both yeast and *Drosophila*. Different HP1 isoforms in mammals have been shown to play distinct roles in the differentiation of several cell types (Agarwal et al. 2007; Cammas et al. 2007; Panteleeva et al. 2007; Takanashi et al. 2009). This specificity is also reflected in the high degree of plasticity observed in the sub-nuclear distribution of the different isoforms (Ritou et al. 2007). Given the essential role played by HP1 in the organization of heterochromatic domains, we have used its *in vivo* localization as a marker for the localization of heterochromatin domains in developing *Caenorhabditis elegans* embryos.

C. elegans provides a simple model system to study HP1 localization and dynamics in a cellular and developmental context. The localization of tagged fluorescent proteins can be observed easily in the transparent embryo, and embryos can be manipulated genetically to uncover important regulatory mechanisms. Many of these cellular and molecular mechanisms are conserved from flies to vertebrates. HPL-2 is found localized in a limited number of discrete nuclear foci at embryonic stages, varying around a value of 15 foci per nucleus in 2D maximum projection images (Coustham et al. 2006). The LIN-13 zinc finger protein was found to be required for HPL-2 recruitment in nuclear foci. LIN-13 directly interacts with HPL-2 *in vivo* and co-localizes with HPL-2 in nuclear foci. In the

absence of *lin-13*, HPL-2 was found to be weakly and homogeneously distributed throughout the nucleus. By contrast, LIN-13 localization was found to be independent of HPL-2. Therefore, the specificity of HPL-2 targeting to nuclear domains is imparted at least partly by the presence of the LIN-13 zinc finger protein (Coustham et al. 2006).

hpl-2 and *lin-13* act in the “synMuv” (synthetic multivulval) pathway, which defines redundant negative regulators of a Ras signaling cascade required for vulval induction (Couteau et al. 2002; Coustham et al. 2006). Most other synMuv genes also encode for chromatin-associated proteins involved in transcriptional regulation, including Rb and components of the Mi-2/NuRD and TIP60/NuA4 chromatin remodeling complexes. To a lesser extent, localization studies have shown that other synMuv genes may also influence HPL-2 localization (Coustham et al. 2006). Indeed, the number of HPL-2 foci from 2D maximum projection images was found to increase significantly in the developing embryo in the absence of the NuA4 histone acetylase complex or the type 1 histone deacetylase HDA-1/HDAC1, suggesting that perturbing the dynamic acetylation/deacetylation equilibrium of specific chromosomal regions may either lead to ectopic recruitment of HPL-2 to additional chromosomal sites or result in loss of cohesion of HPL2-bound domains. These results were obtained by counting the number of nuclear HPL-2::GFP foci in nuclei of live embryos in which different synMuv genes had been inactivated by RNA interference (RNAi). To this end, optical sections of HPL-2::GFP embryos containing between 60 and 80 cells were acquired with an epifluorescence microscope. Maximum intensity projections of deconvolved sections were performed and observed with the same dynamic display to count nuclear foci. This manual way of counting revealed differences in the number of HPL-2 foci per nucleus, but was however not adapted to analyze their intranuclear distribution. More importantly, 3D to 2D projection effects can introduce considerable artifacts in foci counts, as demonstrated below. To circumvent these issues, an objective image analysis approach was designed by including an image segmentation step based on the wavelet transform modulus maxima (WTMM) method (Arneodo et al. 2000) applied previously to the segmentation of chromosome territories in interphase nuclei (Brianna

Caddle et al. 2007; Khalil et al. 2007) and ultra-thin gold aggregates (Roland et al. 2009).

In this study, the WTMM method was adapted to segment nuclei of *C. elegans* embryos in three dimensions, based on the HPL2::GFP fluorescence background. This new image analysis method allowed a complete re-examination of a large data set, thus revealing additional information on the nuclear positioning of these HPL2-bound domains in the developing *C. elegans* embryo in several genetic backgrounds. We found that HPL2 fluorescence tend to localize at the 3D nuclear periphery and that this trend was dramatically increased in one of the mutants analyzed. Importantly, a probabilistic model was also developed and numerical simulations were run to provide robust evidence that the 3D positioning of foci within the cell nucleus has a dramatic effect on the number of foci previously identified in the 2D maximum projection from the same image stacks. In particular, it is demonstrated that two nuclei having the same number of foci, but with a different 3D positioning scheme, can have significantly different counts in the 2D maximum projection.

Materials and methods

C. elegans strains and RNAi

Experimental procedures had been described in a previous paper (Coustham et al. 2006). Briefly, embryos expressing *hpl-2::GFP* were dissected from gravid mothers derived either from L1 larvae grown on RNAi feeding plates (Kamath and Ahringer 2003), or from injected L4 larvae (Fire et al. 1998). RNAi treatment produced the same post-embryonic phenotypes previously described, confirming its efficacy (Kamath and Ahringer 2003). No obvious embryonic defects were observed. Embryos were mounted on fresh 4% agar pads in M9.

HPL2::GFP acquisition and deconvolution

To compare foci positioning in equivalent conditions, analyses were restricted to embryos containing between 60–80 cells. Parameters of image acquisition, restoration and analysis were kept constant for embryos issued from various genetic backgrounds obtained by RNAi (*lin-13*,

lin-35, *lin-9*, *mep-1*, *let-418*, *hda-1*, *mys-1*, *trr-1*, *lin-53*). Image stacks of whole HPL2::GFP embryos were acquired with a band pass GFP filter every 300 nm, using the $\times 63$ objective lens (NA=1.4) of a motorized Zeiss Axioplan2 fluorescence microscope, equipped with a Coolsnap HQ camera, driven by Metamorph (v. 6.3), without binning (1 pixel=102 nm). The 3D point spread function of our system was measured with fluorescent microspheres to restore the image stacks using a deconvolution procedure available as a plugin in Metamorph. The Richardson and Lucy algorithm was used to deconvolve each stack using 100 iterations.

Image segmentation with the WTMM method on raw image stacks

Image segmentation with continuous wavelets is based on the derivative of a 2D smoothing function (Gaussian filter) acting as an “edge detector” (Arneodo et al. 2000). Let

$$\Phi_{\text{GAU}}(x, y) = \exp\left(-\frac{|\mathbf{x}|^2}{2}\right) \quad (1)$$

where $|\mathbf{x}| = \sqrt{(x^2 + y^2)}$, be the Gaussian function so that

$$\Psi_1(x, y) = \partial\Phi_{\text{GAU}}(x, y)/\partial x \quad \text{and} \quad (2)$$

$$\Psi_2(x, y) = \partial\Phi_{\text{GAU}}(x, y)/\partial y$$

are defined as the partial derivatives with respect to x and y . For any 2D function f (i.e., an image), the continuous wavelet transform (WT) of f with respect to Ψ_1 and Ψ_2 has two components:

$$T_{\Psi_1}[f] = \frac{1}{a^2} \int d^2 \mathbf{x} \Psi_1\left(\frac{\mathbf{x} - \mathbf{b}}{a}\right) f(\mathbf{x}) \quad \text{and} \quad (3)$$

$$T_{\Psi_2}[f] = \frac{1}{a^2} \int d^2 \mathbf{x} \Psi_2\left(\frac{\mathbf{x} - \mathbf{b}}{a}\right) f(\mathbf{x})$$

where \mathbf{b} and a represent parameters of position and scale respectively. The WT is therefore the gradient vector of $f(\mathbf{x})$ smoothed by dilated versions of the Gaussian filter $\Phi_{\text{GAU}}(\mathbf{x}/a)$. The WT can be written in polar coordinates, i.e., in terms of its modulus and argument:

$$\mathbf{T}_{\Psi}[f](\mathbf{b}, a) = (\mathbf{M}_{\Psi}[f](\mathbf{b}, a), \mathbf{A}_{\Psi}[f](\mathbf{b}, a)) \quad (4)$$

where

$$\begin{aligned} M_{\Psi}[f](b, a) &= \sqrt{(T_{\Psi_1}[f]^2 + T_{\Psi_2}[f]^2)} \text{ and} \\ A_{\Psi}[f](b, a) &= \text{Arg}(T_{\Psi_1}[f] + iT_{\Psi_2}[f]). \end{aligned} \quad (5)$$

At each size scale a , the WTMM or intensity gradient maxima are defined by the positions where the modulus of the WT, $(M_{\Psi}[f](b, a))$, is locally maximal. These WTMM are automatically organized as maxima chains, which act as contour lines of the smoothed image at the considered scales. At a given scale, the algorithm scans all the boundary lines that correspond to the highest values of the gradient, i.e., the maxima chains. The algorithm then keeps only those maxima chains that are connected, consistent with the nuclear border we want to detect (see Fig. 1). This process is repeated for all size scales (limited by the resolution of the microscope). For a detailed description, the reader is referred to a previous work (Khalil et al. 2007).

Statistical radial distribution of HPL-2-GFP foci on deconvolved image stacks

A spherical shell intensity algorithm was used to characterize the radial distribution of the foci from the deconvolved images. This type of algorithm has been widely used in the study of cell architecture (for example, see (Cremer et al. 2001)). In short, each sphere corresponding to the embryonic nuclei is divided into shells of thickness 100 nm. For each shell, the average intensity of the voxels is calculated to produce the charts shown in Fig. 5. For a nucleus containing foci positioned following a uniform random distribution, a flat average intensity distribution is expected (see the black curve corresponding to *lin-13* in Fig. 5) while for a nucleus with foci having a preferential radial position towards the periphery, an average intensity distribution with a peak at large radius values is expected. Note that regardless of the type of preferential position nomenclature, all distribution curves are expected to decrease for large values of the radius (approaching the edge of the nucleus) since the foci themselves have a non-negligible volume, only a small fraction of which can lie at the extreme periphery of the nucleus.

Probabilistic modeling

A probabilistic model was developed to obtain detailed quantitative information on the 3D positioning of foci within the embryonic cell nucleus. Several small spheres, corresponding to the foci, were positioned within a large sphere, corresponding to the cell nucleus, via a probabilistic distribution that is described by a single parameter called the *radial probability*, q , in the following way. The position of the center of each focus is determined randomly via a uniform distribution within the unit sphere. The distance between the center of the focus and the center of the unit sphere is then rescaled by taking it to the power q . Thus for example, if $q=1$, the position of the foci will not be rescaled and it will be randomly positioned (i.e., following a uniform random distribution) within the nucleus; for $q=0$, the foci will be positioned at the very edge of the nucleus (restricting the foci to be completely included in the nucleus); and for $q>1$, the foci will be preferentially positioned towards the center of the nucleus (see Electronic supplementary materials (Figs. S1, S2, S3, S4, and S5) for 3D animations corresponding to five different values of the radial probability). This process is repeated for each small sphere (or foci), making sure that they do not overlap within the nucleus.

Results

In what follows, one of the main hypotheses is that the shape of an embryonic nucleus can be safely approximated by a sphere, which was validated by the careful examination of several x - z , and y - z 2D planes and projections (data not shown—also see (Coustham et al. 2006)).

Reconstructing 3D nuclei from the analysis of 2D raw image sections

Instead of adapting the 3D WTMM method (Kestener and Arneodo 2003, 2004) to perform a direct 3D segmentation of the nuclei, the 2D WTMM segmentation method is used on each z -stack in the image cube. For each one of these 2D x - y planes such as the one presented in Fig. 1a, the nuclei boundaries are segmented from non-deconvolved stacks via the 2D WTMM segmentation method (see “Material and methods” and (Khalil et al.

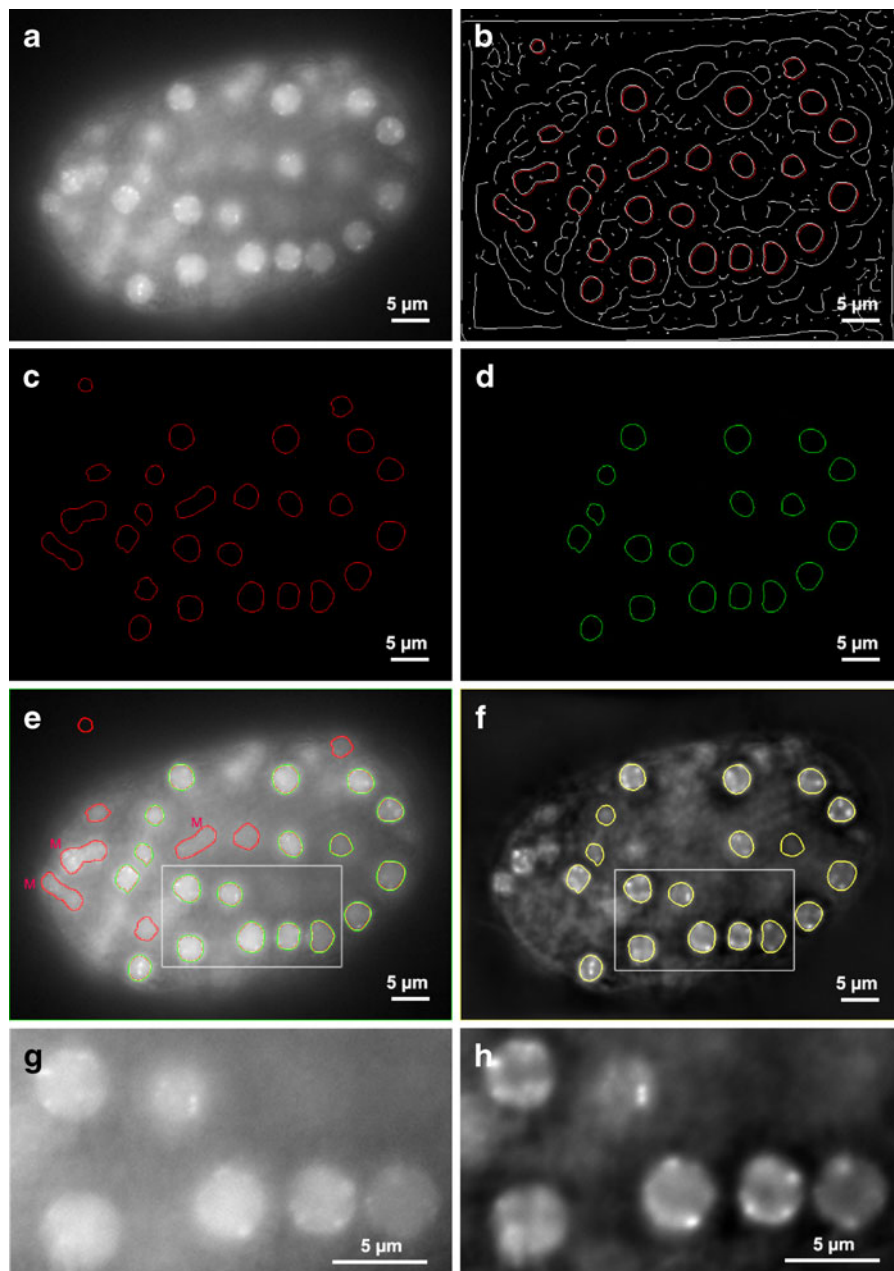


Fig. 1 Automated segmentation of *Caenorhabditis elegans* embryonic nuclei with the WTMM segmentation method. **a** Gray-scale coding of a single raw x - y section from a wild-type HPL-2::GFP embryo imaged with widefield microscopy. The image from (**a**) has been wavelet filtered, and the maxima chains were calculated. This is done at multiple size scales only one of which is represented in (**b**). **c** Only the connected maxima chains (i.e., the *connected segmentation lines* shown in *red* also on **b**) are kept. **d** Only the *connected green lines* satisfying further conditions are kept (see main text as well as Fig. 2 for details). **e** Superimposition of the *connected segmentation lines* (all *lines in red* and retained *lines in yellow*)

with the gray-scale coding of the raw x - y section. The nuclei highlighted with a *yellow line* are kept for analysis, while the nuclei or objects highlighted by a *red line* are discarded from further analysis, like mitotic cells, noted M. **f** The retained *yellow segmentation lines* are then transferred to the corresponding deconvolved 2D section to analyze fluorescence intensity distribution within every individual nuclei (following the 3D sphere reconstruction, see text and Fig. 3) by using the spherical shell intensity algorithm. **g** Enlarged sub-region of the raw section displayed in (**e**). **h** Enlarged sub-region of the deconvolved section displayed in (**f**)

2007)), as shown in Fig. 1b, c. Spurious segmentation lines corresponding to serendipitously organized noisy regions or other regions that do not correspond to actual nuclei (for e.g., outside of the embryo) must be eliminated to obtain Fig. 1d (see also red lines on Fig. 1e). Additionally, connected detection lines having a filament index (which, for an ellipse is the ratio between the long and short axes, (Khalil et al. 2007)) that is greater than 1.5 were also rejected, as being very likely associated to mitotic cells (see cells noted M on Fig. 1e).

Unlike chromosome territories (Brianna Caddle et al. 2007; Khalil et al. 2007) and ultra-thin gold aggregates (Roland et al. 2009), for which the wavelet-based segmentation was made as the smallest possible size scale for each object, the segmentation of *C. elegans* nuclei is made at a range of preferential size scales that are defined by the similar sizes of the nuclei. By plotting the number of connected edge detection lines in a 2D x - y plane as a function of the scale parameter (Fig. 2, dark bars), the presence of a preferential scale is detected at $\sim 4.5 \mu\text{m}$, which is well within the range of the diameter of *C. elegans* embryonic cells (ranging from $\sim 11 \mu\text{m}$ in the early

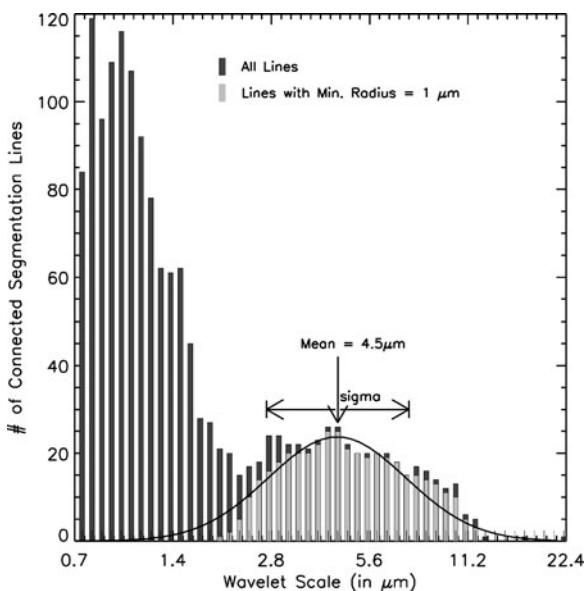


Fig. 2 Histogram of the number of *connected segmentation lines* as a function of the scale parameter a . The *dark bars* correspond to the distribution of all connected segmentation lines except those corresponding to mitotic cells (see text and Fig. 1e for illustration), while the *light bars* result from restricting the algorithm to keep only connected segmentation lines having a radius greater than $1 \mu\text{m}$

embryo to $\sim 3 \mu\text{m}$ in later stages). To best determine which size scales to consider for the segmentation, a minimum radius of $1 \mu\text{m}$ was imposed to the WTMM segmentation lines (Fig. 2, light bars), which yields a distribution that is well approximated by a Gaussian distribution with mean and standard deviation. This restriction does not undermine the quality of the segmentation, due to lower z resolution ghosting effects, as discussed below (see also Fig. 4). The algorithm then considers all connected edge detection lines obtained at the scale given by the mean of the Gaussian distribution and then scans all the size scales in the interval (mean \pm standard deviation) in order to find objects that might not have been detected at the mean scale.

Once each x - y plane in the image stack has been analyzed via the above algorithm (Fig. 3, top), a 3D reconstruction is implemented by fitting spheres (Fig. 3, bottom) to organized groups of edge detection lines (Fig. 3, middle). An algorithm automatically categorizes each of these groups (i.e., one group corresponds to one nucleus) following three conditions: (1) each group must have a sufficient number of edge detection lines, (2) the average intensity must be sufficiently high, and (3) the average gradient along these edge detection lines (given by the modulus of the wavelet transform) must also be sufficiently high. A simple and conservative way of implementing these conditions is to only keep nuclei that have a value that is greater than the mean for each of these three conditions. This is done automatically in the algorithm.

One advantage of choosing 3D widefield fluorescence microscopy over confocal microscopy is to collect the maximum of light, which for low light intensity and low signal to noise samples turns out to be crucial. The counter reality of 3D widefield fluorescence microscopy is an increased fluorescence blur in the z -axis, which is reflected by very faint ghost regions in z above and below a cell nucleus. As shown on Fig. 4, the sensitive WTMM segmentation method is able to detect them. An additional algorithm is implemented to detect the 2D segmentation line having maximal size and average gradient value via a ranking system. The area formed by this closed critical segmentation line is used to determine the radius of the sphere that represents the nucleus, so that for each nucleus in an embryo, the (x, y, z) coordinates and radius are obtained, thus setting up the next step of the analysis on the deconvolved images.

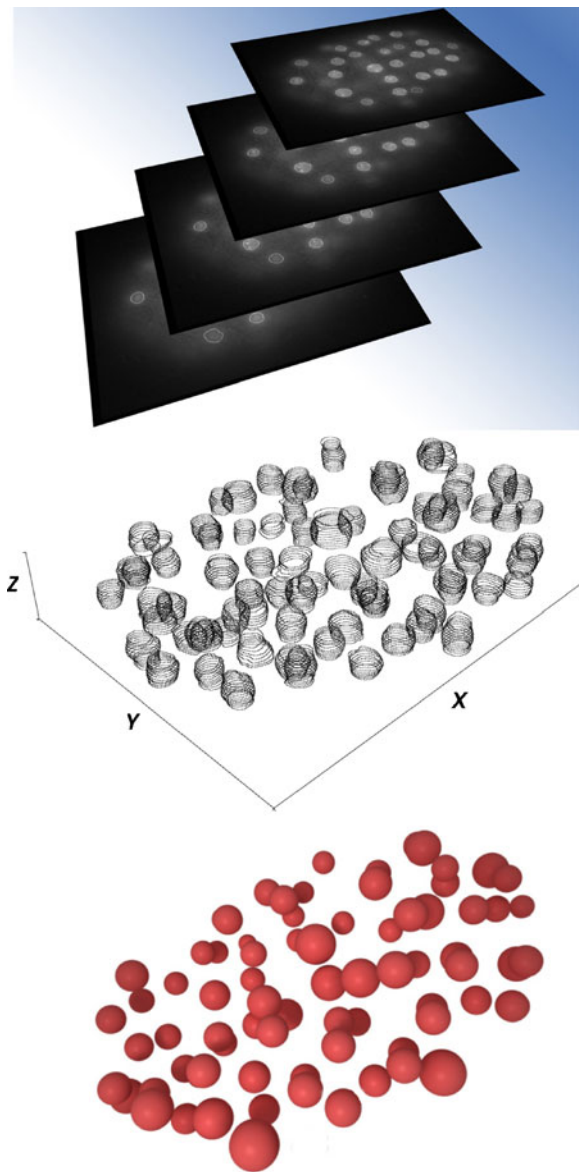


Fig. 3 The wavelet transform modulus maxima segmentation is run on all individual x - y sections for each embryo (*top*). Connected segmentation lines are appropriately positioned in 3D space (*middle*) and are categorized into groups according to the proximity of their geometrical center. Those groups that satisfy the automated algorithmic conditions correspond to cell nuclei (see text) and are fitted with a sphere (*bottom*)

Characterization of the radial distribution of sub-nuclear HPL-2-GFP foci

An increasing-radius shell algorithm (see “[Material and methods](#)”) was used on the deconvolved image stacks to obtain the averaged radial distribution

curves shown in Fig. 5 for every genotype. For comparison purposes, all curves were displayed on the same graph starting at the same origin. To quantify the information contained in these distribution curves, the slope of an imaginary straight line joining the peak of the curve and its value at radius 0 was calculated. To obtain a detailed statistical analysis of quantitative significant differences between the genotype, the slopes were averaged over all curves corresponding to all of the nuclei associated to each genotype. These results, together with p values obtained from the Student’s t test when comparing each mutant to the wild-type embryos are listed in Table 1, where the relative positions of the curve peaks are also listed. A bar chart representing the average slope for each genotype is presented in Fig. 6. Four categories of preferential foci positioning schemes appear to emerge from the analyzed data sets: (1) No preferential positioning (*lin-13*, black in Figs. 5 and 6); (2) weak preferential positioning (WT, *lin-9*, *lin-35*, *lin-53*, red in Figs. 5 and 6); (3) strong preferential positioning (*mep-1*, *hda-1*, *let-418*, *mys-1*, blue in Figs. 5 and 6); and (4) very strong preferential positioning (*trr-1*, green in Figs. 5 and 6).

Probabilistic modeling: 3D positioning strongly influences 2D maximum projection counts

A simple probabilistic model is introduced, in which small spheres corresponding to GFP-tagged foci are positioned into a larger sphere corresponding to an embryonic cell nucleus. The positions of the foci are determined from a uniform random distribution within the nucleus, except that their distance from the center of the nucleus is altered via the radial probability parameter q (see “[Material and methods](#)”). Note that for $q=1$, no alterations are introduced whereas when q becomes smaller the foci are attracted towards the periphery of the nucleus, with all foci directly at the periphery for $q=0$. The simulation was run for one million iterations for 100 different values of q between $q=0$ and $q=1$ (i.e., in increments of 0.01), for a total of 100 million runs. The size parameters were taken from empirical data, with a nuclear radius of 2.5 μm and foci radii taken from a normal distribution with a mean \pm standard deviation of 250 ± 50 nm. Sample 3D animations corresponding to five different values of q are shown in the

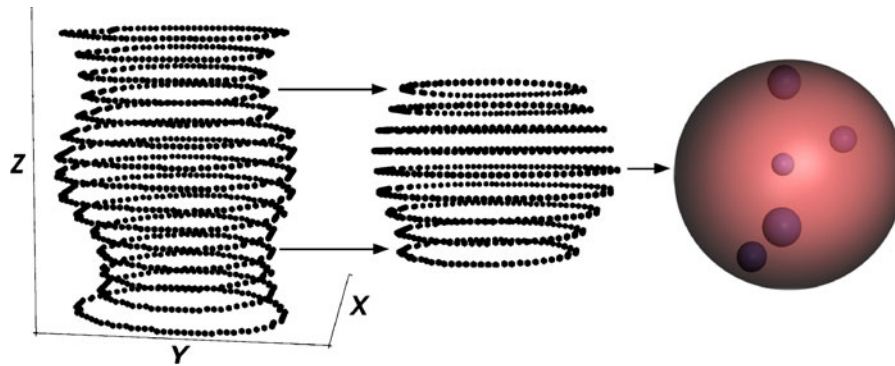


Fig. 4 Fluorescence ghosting. The WTMM segmentation method is sensitive enough to detect weak fluorescent signals from ghost objects on planes that have no actual nucleus boundary on them. The segmentation lines corresponding to

these ghost objects that result artificially from diffusing fluorescence have very low gradient values and are therefore easily removed (see text)

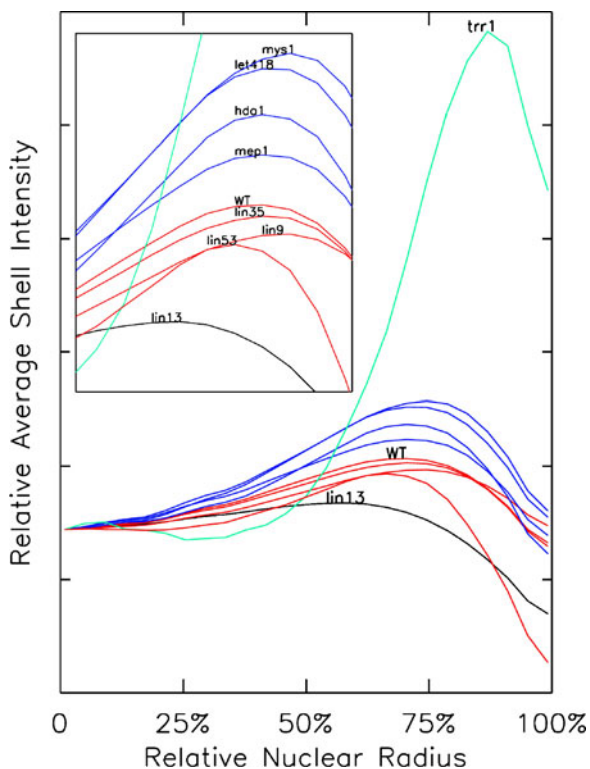


Fig. 5 Average shell intensity as a function of the relative nuclear radius, with 0 being the center of the nuclei. For all genotypes, the average curves are shown. For comparison purposes, all curves are displayed on the same graph starting at the same origin. This plot evidences four categories of preferential peripheral positioning: (1) No preferential positioning (*lin-13*, black); (2) weak preferential positioning (*WT*; *lin-9*, *lin-35*, *lin-53*, red); (3) strong preferential positioning (*mep-1*, *hda-1*, *let-418*, *mys-1*, blue); and (4) very strong preferential positioning (*trr-1*, green)

Electronic supplementary materials (Figs. S1, S2, S3, S4, and S5). Figure 7 shows how a fixed number of foci randomly positioned in a simulated nucleus, but with a radial distance that is altered by the radial probability parameter q , can have dramatically different counts in the 2D maximum projection, ranging from 19 to 14. Note that the range of 2D foci counts obtained from this rigorous simulation (where it is important to emphasize that the number of foci simulated in the 3D nucleus was kept constant for each value of the parameter q) is approximately the same as what was found previously from manual counts on empirical data (see Fig. 6 in (Coustham et al. 2006)).

Discussion

The 2D WTMM segmentation method is a multi-scale analysis formalism that was first introduced to perform accurate object segmentation of a specific number of mouse chromosome territories (Khalil et al. 2007). The methodology was generalized to segment any number of objects when characterizing ultra-thin gold aggregates from atomic force microscopy (Roland et al. 2009). In order to obtain an objective segmentation of *C. elegans* embryonic nuclei, the WTMM segmentation method was further generalized to segment any number of objects in three dimensions. This allowed us to investigate the three-dimensional radial positioning of GFP fluorescence associated with HPL-2/HP1 foci. By this method, a preferential positioning of fluorescence was observed

Table 1 Preferential peripheral positioning for each genotype

Genotype	Number of nuclei	Average slope	5% confidence error	Comparison to wild type: $\text{Log}_{10}(p \text{ value})$	Average relative peak position (% of nuclear radius)
<i>lin-13</i>	163	209	21	-28.8	54.2
WT	676	442	30	-	64.4
<i>lin-35</i>	269	422	35	-0.7	64.7
<i>lin-9</i>	255	349	26	-5.2	70.4
<i>lin-53</i>	27	473	167	-0.4	56.2
<i>mep-1</i>	204	599	65	-4.5	64.0
<i>let-418</i>	274	708	54	-14.8	64.3
<i>hda-1</i>	87	726	101	-5.6	63.8
<i>mys-1</i>	141	719	66	-11.1	71.6
<i>trr-1</i>	39	2,524	500	-9.5	85.5

at the nuclear periphery for every genotype examined, except for *lin-13*, in which nuclear foci are no longer observed (Coustham et al. 2006). The degree to which HPL2 fluorescence is preferentially positioned at the periphery correlates with the number of foci counts from 2D maximum projections published elsewhere (Coustham et al. 2006). Importantly, the development of a probabilistic model unambiguously shows that different 3D positioning schemes of

different peripheral preference (of the same number of foci) can lead to considerably different counts in the 2D maximum projections (see Fig. 7).

In wild-type embryonic nuclei, a weak preference for HPL-2/HP1 fluorescence at the nuclear periphery is observed with a maximum fluorescence intensity peak observed at $\sim 64\%$ of the nuclear radius and a slope of 442 ± 30 , which contrasts with a much lower slope of 209 ± 21 for the *lin-13* mutant, considered as

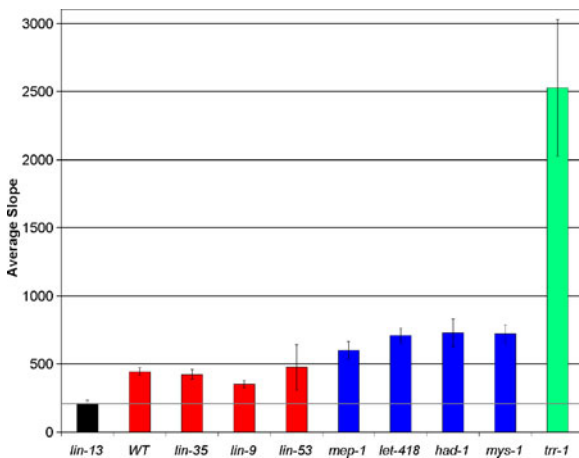


Fig. 6 Bar chart showing the average slopes for each genotype. Each slope is obtained by taking the average over all nuclei and all embryos per genotype, with error bars corresponding to the 5% confidence interval. These results, together with p values obtained from the student's t test when comparing each mutant to the wild-type embryos are listed in Table 1. The color coding for each of the four positioning categories is the same as in Fig. 5. A horizontal gray bar was added, corresponding to the average slope of the *lin-13* curves, considered as the reference for homogeneous noisy background

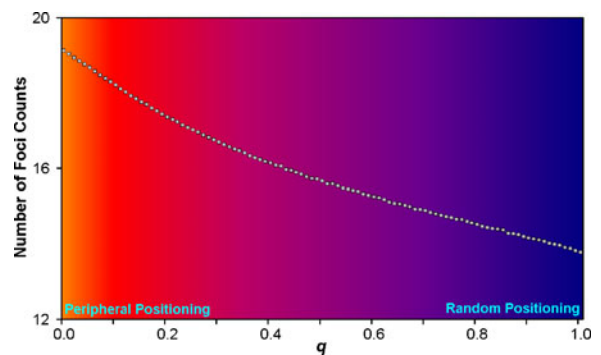


Fig. 7 Probabilistic model: Foci count in the 2D maximum projection as a function of the radial probability parameter q . A value for q of 1 corresponds to a random distribution of the spheres, while a value of 0 corresponds to perinuclear positioning. One million simulations were run for each value of q between 0 and 1 in increments of 0.01, for a total of 100 million runs. For each run, a fixed number of 45 artificial foci were positioned in the simulated nucleus. The radius of the nucleus was $2.5 \mu\text{m}$ and the foci radii were taken from a normal distribution with mean \pm sigma of $250 \pm 50 \text{ nm}$, as suggested from empirical data. These simulation counts can be compared with experimental counts published previously (Coustham et al. 2006)

the reference for noisy background. Several studies suggest that chromatin at the nuclear periphery is generally hypoacetylated. Inhibition of HDACs with trichostatin A (TSA) has been shown to alter this acetylation state (Taddei et al. 2001; Gilchrist et al. 2004) and peripheral positioning of selected loci and chromosomes within interphase nuclei has been found to correlate with a lower level of acetylation (Strasak et al. 2009).

Since components of the nuclear periphery are likely to have affinity for chromatin marked with specific histone modifications, histone variants, or other chromatin-associated proteins, treatments such as TSA, through hyperacetylation of chromatin and other proteins, is likely to modify these interactions. This chemical treatment previously found to relocate heterochromatin at the nuclear periphery was associated with a loss of HP1 (Taddei et al. 2001). We found five genetic backgrounds (*mep-1*, *let-418*, *hda-1*, *mys-1* and *trr-1 RNAi*) where HPL-2/HP1 remained concentrated in nuclear foci (Coustham et al. 2006) while being displaced even more at the nuclear periphery (see Figs. 5 and 6; Table 1). Although these studies differ in the approach and interpretation of the results made, they highlight how HP1 domains can be used as reference markers of the intranuclear state in various species.

We have found that abrogating the activity of factors associated with chromatin remodeling or histone modifications by RNAi can alter the nuclear localization of HPL-2/HP1. This effect is most dramatic upon inhibition of *trr-1*, the *C. elegans* homologue of transformation/transcription domain-associated protein (TRRAP) and its yeast homologue Tra1. As common components of many histone acetyltransferase (HAT) complexes, the TRRAP and Tra1 appear to be the only components through which HAT complexes (either histone H3 acetylating complexes or those with preference for histone H4) contact transcription activators (Brown et al. 2001; Bhaumik et al. 2004). TRRAP-related proteins share homology with the phosphatidylinositol-3-kinase (PI3K) family members. However, since TRRAP does not appear to possess kinase activity, it is thought that it may instead serve as an adaptor/scaffold for protein–protein interaction and multiprotein assemblies or as a platform for recruitment of different HAT and non-HAT complexes to chromatin (Murr et al. 2007). The dramatic relocation of HPL-2/HP1 chromatin domains at the

nuclear periphery in the absence of *trr-1*/TRRAP may therefore result from increased hypoacetylation in the absence of targeted HAT activity.

In mammalian cells, prolonged treatment with a low concentration of TSA results in histone hyperacetylation at the nuclear periphery, which is not a feature of heterochromatin (Taddei et al. 2005). Notably, constitutive heterochromatic regions, as defined by their late replication timing and HP1 enrichment, are excluded from this hyperacetylated domain. Whether inhibition of HAT activity would have the opposite consequences, e.g., increase HP1 binding, has not been tested.

C. elegans lacks constitutive heterochromatic regions, as defined by pericentromeric regions, and the chromatin domains bound by HPL-2/HP1 remain to be defined. Furthermore, it is not clear to what extent H3K9 methylation contributes to HPL-2 binding, as nuclear foci are completely lost in the absence of the *lin-13* zinc finger protein. Increased hypoacetylation may result in a chromatin structure at the nuclear periphery more favorable to HPL-2/HP1 recruitment.

Interfering with *hda-1* activity by RNAi results in a higher average shell intensity at the nuclear periphery compared with wild-type embryos, but has a much less pronounced effect of HPL-2/HP1 intranuclear localization compared to *trr-1*/TRRAP (Figs. 5 and 6). Since *hda-1* is only one of five HDACs present in *C. elegans*, its inhibition by RNAi may have a less dramatic effect on genome-wide acetylation compared to *trr-1* inhibition. Alternatively, *trr-1*/TRRAP inactivation may influence nuclear organization by both HAT dependent and independent mechanisms, as already described for mammalian cells (Murr et al. 2007).

lin-35/Rb, *lin-9* and *lin-53*/RbAp are components of the Drosophila and mammalian dDREAM complex, which functions to repress cell cycle-dependent genes (Lipsick 2004). Consistent with these genes playing a role in the repression of specific genes, we failed to see any significant change in HPL2::GFP localization upon their inactivation by RNAi (see Figs. 5 and 6; Table 1). MEP-1, LET-418/Mi-2, and HDA-1 physically interact in a complex similar to the mammalian Mi-2/NuRD complex required for transcriptional repression in certain contexts. Nonetheless, at least some enzymes capable of modifying chromatin states localize to zones that promote repression such as heterochromatin. In cultured mammalian cells, NuRD, can be found both at the

nuclear periphery and associated with centromeric satellite repeats. *mep-1*, *let-418*, and *hda-1* RNAi results in a slight increase in the peripheral localization of HPL-2, perhaps reflecting a more global effect on nuclear organization.

Finally, although biochemical studies have failed to detect HP1 as a component of either dREAM- or Rb-related complexes in *C. elegans*, Drosophila or mammalian cells, we cannot exclude that the changes in HPL-2/HP1 localization observed in these studies reflect at least partly the disruption of transient interactions between these proteins.

The overarching goal of this paper was to revisit a statistically large sample of imaging data of developing embryonic *C. elegans* nuclei in different genotypic contexts (Coustham et al. 2006). The WTMM segmentation method (Khalil et al. 2007; Roland et al. 2009) was generalized and adapted to segment the cell nuclei and a radial distribution algorithm was implemented to characterize the preferential peripheral positioning of HPL-2/HP1. For all genotypes except *lin-13*, a preferential foci positioning at the peripheral nucleus was shown and quantified. A probabilistic 3D cell nuclear model was also developed and run in order to demonstrate the deceptive limitations of using a technique of 2D maximum projection foci counts. Taken together, these results give new evidence of the crucial need to implement and use accurate 3D image analysis techniques to adequately characterize 3D foci distributions. Applied systematically, these computational techniques of live cell image analysis and modeling constitute a powerful assay to screen for factors influencing nuclear architecture through the intranuclear positioning of specific domains.

Acknowledgments A.K. acknowledges the University of Maine new faculty startup funds as well as a grant from the Maine Cancer Foundation. C.V. is supported through a NSF-funded Research Experiment for Undergraduate at the University of Maine, NSF Fund CCF #0754951. The microscopy acquisition was realized on the Microscope Facility of IFR128 Biosciences Gerland-Lyon Sud, PLATIM. K.M. benefited from a fellowship from La Ligue Contre le Cancer.

References

- Agarwal N, Hardt T, Brero A et al (2007) MeCP2 interacts with HP1 and modulates its heterochromatin association during myogenic differentiation. *Nucleic Acids Res* 35 (16):5402–5408
- Arneodo A, Decoster N, Roux S (2000) A wavelet-based method for multifractal image analysis. I. Methodology and test applications on isotropic and anisotropic random rough surfaces. *European Journal of Physics B* 15:567–600
- Bhaumik SR, Raha T, Aiello DP, Green MR (2004) In vivo target of a transcriptional activator revealed by fluorescence resonance energy transfer. *Genes Dev* 18(3):333–343
- Brianna Caddle L, Grant JL, Szatkiewicz J et al (2007) Chromosome neighborhood composition determines translocation outcomes after exposure to high-dose radiation in primary cells. *Chromosome Res* 15(8):1061–1073
- Brown CE, Howe L, Sousa K et al (2001) Recruitment of HAT complexes by direct activator interactions with the ATM-related Tra1 subunit. *Science* 292(5525):2333–2337
- Buhler M, Gasser SM (2009) Silent chromatin at the middle and ends: lessons from yeasts. *EMBO J* 28(15):2149–2161
- Cammass F, Janoshazi A, Lerouge T, Losson R (2007) Dynamic and selective interactions of the transcriptional corepressor TIF1 beta with the heterochromatin protein HP1 isoforms during cell differentiation. *Differentiation* 75(7):627–637
- Chaly N, Munro SB (1996) Centromeres reposition to the nuclear periphery during L6E9 myogenesis in vitro. *Exp Cell Res* 223(2):274–278
- Cook PR, Marenduzzo D (2009) Entropic organization of interphase chromosomes. *J Cell Biol* 186(6):825–834
- Coustham V, Bedet C, Monier K, Schott S, Karali M, Palladino F (2006) The *C. elegans* HP1 homologue HPL-2 and the LIN-13 zinc finger protein form a complex implicated in vulval development. *Dev Biol* 297(2):308–322
- Couteau F, Guerry F, Muller F, Palladino F (2002) A heterochromatin protein 1 homologue in *Caenorhabditis elegans* acts in germline and vulval development. *EMBO Rep* 3(3):235–241
- Cremer T, Kreth G, Koester H et al (2000) Chromosome territories, interchromatin domain compartment, and nuclear matrix: an integrated view of the functional nuclear architecture. *Crit Rev Eukaryot Gene Expr* 10(2):179–212
- Cremer M, von Hase J, Volm T et al (2001) Non-random radial higher-order chromatin arrangements in nuclei of diploid human cells. *Chromosome Res* 9(7):541–567
- de Nooijer S, Wellink J, Mulder B, Bisseling T (2009) Non-specific interactions are sufficient to explain the position of heterochromatic chromocenters and nucleoli in interphase nuclei. *Nucleic Acids Res* 37(11):3558–3568
- Dundr M, Misteli T (2001) Functional architecture in the cell nucleus. *Biochem J* 356(Pt 2):297–310
- Fang Y, Spector DL (2005) Centromere positioning and dynamics in living Arabidopsis plants. *Mol Biol Cell* 16 (12):5710–5718
- Ferguson M, Ward DC (1992) Cell cycle dependent chromosomal movement in pre-mitotic human T-lymphocyte nuclei. *Chromosoma* 101(9):557–565
- Fire A, Xu S, Montgomery MK, Kostas SA, Driver SE, Mello CC (1998) Potent and specific genetic interference by double-stranded RNA in *Caenorhabditis elegans*. *Nature* 391(6669):806–811
- Gilbert N, Gilchrist S, Bickmore WA (2005) Chromatin organization in the mammalian nucleus. *Int Rev Cytol* 242:283–336

- Gilchrist S, Gilbert N, Perry P, Bickmore WA (2004) Nuclear organization of centromeric domains is not perturbed by inhibition of histone deacetylases. *Chromosome Res* 12(5):505–516
- Kamath RS, Ahringer J (2003) Genome-wide RNAi screening in *Caenorhabditis elegans*. *Methods* 30(4):313–321
- Kestener P, Arneodo A (2003) Three-dimensional wavelet-based multifractal method: the need for revisiting the multifractal description of turbulence dissipation data. *Phys Rev Lett* 91(19):194501
- Kestener P, Arneodo A (2004) Generalizing the wavelet-based multifractal formalism to random vector fields: application to three-dimensional turbulence velocity and vorticity data. *Phys Rev Lett* 93(4):044501
- Khalil A, Grant JL, Caddle LB, Atzema E, Mills KD, Arneodo A (2007) Chromosome territories have a highly nonspherical morphology and nonrandom positioning. *Chromosome Res* 15(7):899–916
- Lipsick JS (2004) synMuv verite–Myb comes into focus. *Genes Dev* 18(23):2837–2844
- Murr R, Vaissiere T, Sawan C, Shukla V, Herceg Z (2007) Orchestration of chromatin-based processes: mind the TRRAP. *Oncogene* 26(37):5358–5372
- Panteleeva I, Boutillier S, See V et al (2007) HP1alpha guides neuronal fate by timing E2F-targeted genes silencing during terminal differentiation. *Embo J* 26(15):3616–3628
- Ritou E, Bai M, Georgatos SD (2007) Variant-specific patterns and humoral regulation of HP1 proteins in human cells and tissues. *J Cell Sci* 120(Pt 19):3425–3435
- Roland T, Khalil A, Tanenbaum A et al (2009) Revisiting the physical processes of vapodeposited thin gold films on chemically modified glass by atomic force and surface plasmon microscopies. *Surface Science* 603:3307–3320
- Solovei I, Schermelleh L, Doring K et al (2004) Differences in centromere positioning of cycling and postmitotic human cell types. *Chromosoma* 112(8):410–423
- Strasak L, Bartova E, Harnicarova A, Galiova G, Krejci J, Kozubek S (2009) H3K9 acetylation and radial chromatin positioning. *J Cell Physiol* 220(1):91–101
- Taddei A (2007) Active genes at the nuclear pore complex. *Curr Opin Cell Biol* 19(3):305–310
- Taddei A, Maison C, Roche D, Almouzni G (2001) Reversible disruption of pericentric heterochromatin and centromere function by inhibiting deacetylases. *Nat Cell Biol* 3(2):114–120
- Taddei A, Roche D, Bickmore WA, Almouzni G (2005) The effects of histone deacetylase inhibitors on heterochromatin: implications for anticancer therapy? *EMBO Rep* 6(6):520–524
- Takanashi M, Oikawa K, Fujita K, Kudo M, Kinoshita M, Kuroda M (2009) Heterochromatin protein 1gamma epigenetically regulates cell differentiation and exhibits potential as a therapeutic target for various types of cancers. *Am J Pathol* 174(1):309–316
- Vourc'h C, Taruscio D, Boyle AL, Ward DC (1993) Cell cycle-dependent distribution of telomeres, centromeres, and chromosome-specific subsatellite domains in the interphase nucleus of mouse lymphocytes. *Exp Cell Res* 205(1):142–151
- Ye Q, Callebaut I, Pezhman A, Courvalin JC, Worman HJ (1997) Domain-specific interactions of human HP1-type chromodomain proteins and inner nuclear membrane protein LBR. *J Biol Chem* 272(23):14983–14989